Signal Processing: Image Communication 123 (2024) 117087

Contents lists available at ScienceDirect

Signal Processing: Image Communication

journal homepage: www.elsevier.com/locate/image

Prediction-based coding with rate control for lossless region of interest in pathology imaging

Joan Bartrina-Rapesta [a,1,*], Miguel Hernández-Cabronero [a,1,2], Victor Sanchez [b,2], Joan Serra-Sagristà [a,1], Pouya Jamshidi [c], J. Castellani [c]

[a] Department of Information and Communications Engineering, Universitat Autónoma de Barcelona, Edifici Q, Carrer de les Sitges, Cerdanyola del Vallés, Barcelona, E-08193, Spain
[b] Department of Computer Science, University of Warwick, Coventry, CV4 7AL, United Kingdom
[c] Department of Pathology, Feinberg School of Medicine at the Northwestern University, 420 E Superior St, Chicago, IL 60611, United States

ARTICLE INFO

Keywords:
Digital pathology images
Region of interest coding
Rate control

ABSTRACT

Online collaborative tools for medical diagnosis produced from digital pathology images have experimented an increase in demand in recent years. Due to the large sizes of pathology images, rate control (RC) techniques that allow an accurate control of compressed file sizes are critical to meet existing bandwidth restrictions while maximizing retrieved image quality. Recently, some RC contributions to Region of Interest (RoI) coding for pathology imaging have been presented. These encode the RoI without loss and the background with some loss, and focus on providing high RC accuracy for the background area. However, none of these RC contributions deal efficiently with arbitrary RoI shapes, which hinders the accuracy of background definition and rate control. This manuscript presents a novel coding system based on prediction with a novel RC algorithm for RoI coding that allows arbitrary RoIs shapes. Compared to other methods of the state of the art, our proposed algorithm significantly improves upon their RC accuracy, while reducing the compressed data rate for the RoI by 30%. Furthermore, it offers higher quality in the reconstructed background areas, which has been linked to better clinical performance by expert pathologists. Finally, the proposed method also allows lossless compression of both the RoI and the background, producing data volumes 14% lower than coding techniques included in DICOM, such as HEVC and JPEG-LS.

1. Introduction

Digital pathology imaging, also known as whole-slide imaging (WSI), has been boosted by novel research in cancer diagnosis [1], software tools that determine automatically whether an image needs to be re-scanned [2], as well as recent computer-aided diagnosis methods [3]. The combination of WSI and these software tools makes essential the close collaboration between researchers, pathologists, and computer scientists. Telepathology technologies are common in collaborative tools because they facilitate transmission, remote visualization and analysis of pathology images. For this reason, the use of telepathology applications for remote visualization and analysis has been established in several laboratories for clinical, research and educational purposes [4–8].

The scanners used in digital pathology generate very high-resolution images, outputting large data volumes as a result. Due to their size, it is not practical or even feasible to transmit all image regions at full resolution. Instead, current telepathology systems perform partial transmission in a three-step process. First, the system transmits a low-resolution version of the WSI, adequate for fast transmission even over slow connections. Second, the specialist selects the regions of interest

* Corresponding author.
E-mail address: joan.bartrina@uab.cat (J. Bartrina-Rapesta).

[1] This work was supported in part by the Spanish Ministry of Science and Innovation (MICINN) and by the European Regional Development Fund (FEDER), funded by MCIN/AEI/10.13039/501100011033/FEDER, UE, under grants RTI2018-095287-B-I00 and PID2021-125258OB-I00, by the Catalan Government under Grant SGR2021-00643, by Centre National d'Études Spatiales (CNES), and by the postdoctoral fellowship programme Beatriu de Pinós, reference 2018-BP-00008, funded by the Secretary of Universities and Research (Government of Catalonia)
[2] This work was supported in part by the Horizon 2020 programme of research and innovation of the European Union under the Marie Skłodowska-Curie grant agreement #801370.

https://doi.org/10.1016/j.image.2023.117087
Received 20 April 2023; Received in revised form 4 December 2023; Accepted 17 December 2023
Available online 22 January 2024

(RoIs) on which they wish to focus [9], e.g., groups of cells or tissue subregions. Third, the system transmits the selected RoIs with perfect fidelity using lossless compression, and the background regions (BG) with lower fidelity using lossy compression. Users can then add and read annotations, as well as repeating steps two and three for other image areas.

In collaborative telepathology systems, two main aspects must be considered. First, RoIs are more important than the BG for pathologists. Thus, it is paramount to provide an encoding mechanism that differentiates between RoIs and BG. Second, when a RoI is compressed and transmitted over a network, the compressed data size must be small enough to meet the constraints imposed by the network capabilities and transmission time limits. This compressed data is hereafter referred to as the bitstream, and its maximum size under the aforementioned conditions, target bitrate. Generating bitstreams larger than the given bit budget causes their truncation, which can largely penalize the quality of the images reconstructed by the receiver. In turn, transmitting bitstreams smaller than the bit budget (or target bitrate) wastes resources that could be used to improve the image fidelity. Hence, employing mechanisms to accurately meet a target bitrate and optimally distributing the bit budget among RoIs and BG is of utmost importance for maximizing the reconstructed image quality. Such mechanisms are known as rate control (RC) algorithms, and are an essential part of modern image compression algorithms used in digital pathology.

The Digital Image and Communication in Medicine (DICOM) includes some coding techniques in its standard [10], from these techniques only JPEG2000 [11], H.264 [12] and HEVC [13,14] provide RC with RoI coding. Modern video codecs, such as H.264 and HEVC, use methods called block-based predictive transform coding to compress images and videos, which have been proven to be very effective for both lossless and lossy compression of medical images and videos [15–17]. Focusing only on block-based predictive coding techniques, several compression contributions that include RC techniques and differentiate between the RoI and the BG have been proposed in the literature [16,18–27].

Liu et al. [18], Zhou et al. [24], Sanchez [25] describe RC techniques for H.264 and HEVC, but do not support RoI coding. El Sayeh Khalil et al. [23] enables the definition of RoIs in the decoder side, and [19,20,26] use RC techniques to provide higher visual quality for the RoI than the BG. Although these contributions provide some control over the final bitrate, they do not provide support for encoding the RoI losslessly, which is a requirement in many clinical scenarios.

A few techniques have been presented that allow lossless compression of the RoI and lossy coding of the BG for a given image. Chen et al. [16] offers this capability, but it does not provide any mechanisms to accurately meet the target bitrate. To the best of our knowledge, only Sanchez et al. proposed RC techniques that allow lossless RoI and lossy BG coding, while approximating a target bitrate [21,22]. However, their average bitrate errors are of nearly 5%, and their allowed RoI shapes are restricted to the block partitions used by HEVC. In consequence, blocks with small intersections with the RoI must also be encoded losslessly. Therefore, more bits than necessary are devoted to encoding the RoI, which is in detriment of coding efficiency and the overall background reconstruction quality. A comparison of relevant methods for the compression of digital pathology images is provided in Table 1.

Based on the aforementioned limitations in the state of the art, here we present a coding system that includes a novel RC method for lossless RoI and lossy BG coding, with highly accurate target bitrate selection. To achieve these features, we propose a smart predictor that can discriminate between RoI and BG pixels, enabling also arbitrarily shaped RoIs, i.e., any pixel can arbitrarily and individually be marked as RoI or BG. In addition, a novel context modeling for a binary entropy encoder is also introduced, which generates smaller pieces of bitstreams, yielding higher bitrate accuracy and improving the coding performance. The proposed RC method is implemented as an extension of [28]. When evaluated on pathology images and different RoIs, our coding system improves upon the state of the art [21,22] in terms of RC accuracy and overall coding performance. When used for purely lossless compression, it outperforms HEVC and JPEG-LS, the most competitive options included in DICOM. In terms of encoding time, our system is faster than HEVC for purely lossless compression when both are executed on a single thread.

Table 1
Properties of different compression algorithms with capability for Rate Control (RC) or Region of Interest (RoI) coding in the state of the art.

	Year	Prediction based	RC for RoI	RoI lossless	Lossless RoI &BG lossy	Accurate target bitrate
Sanchez et al. [21]	2015	✔	✔	✔	✔	✔
Sanchez et al. [22]	2018	✔	✔	✔	✔	✔
Chen et al. [16]	2013	✔	✔	✔	✔	✘
Liu et al. [18]	2008	✔	✘	✘	✘	✔
Meddeb et al. [19]	2014	✔	✔	✘	✘	✘
Xu et al. [20]	2014	✔	✔	✘	✘	✘
Khalil et al. [23]	2019	✔	✘	✘	✘	✘
Zhou et al. [24]	2020	✔	✘	✘	✘	✔
Sanchez et al. [25]	2021	✔	✘	✘	✘	✔
Liu et al. [26]	2021	✔	✔	✘	✘	✘
Jiang et al. [27]	2023	✘	✘	✔	✔	✔

The rest of the paper is structured as follows: Section 2 reviews key elements of prediction coding techniques. Section 3 presents our coding system, including the proposed RC mechanism. Section 4 provides experimental results. Finally, Section 5 concludes this work.

2. Previous work

Image compression techniques are generally categorized according to how the data is decorrelated. In image compression, decorrelation can be produced through transform or prediction, thus image compression techniques are generally categorized into transform- or prediction-based approaches. Both approaches have been employed in the best-performing compression algorithms in the state of the art. The DICOM standard supports JPEG2000 [29], JPEG-LS, AVC [12], and HEVC as the main alternatives for image data compression. It has been shown that HEVC —based on prediction— outperforms JPEG2000 —based on transform— in terms of lossless compression performance [30–32]. When applied to an individual image, lossless HEVC uses block-wise intra prediction based at pixel-level. In JPEG-LS, this prediction is also performed, but without the block division.

Prediction at the pixel-level decorrelates data by exploiting the redundancy among neighboring pixels. For an image x with I columns, J rows, and K color channels (e.g., red, green and blue), pixel-level prediction estimates the value of each sample $x_{i,j,k}$ using only previously coded neighbors, i.e., the predictor is strictly causal. Given prediction $\widetilde{x}_{i,j,k}$, the residual or prediction error is defined as:

$$\Lambda_{i,j,k} = x_{i,j,k} - \widetilde{x}_{i,j,k}. \quad (1)$$

To control the compressed bitrates, the prediction error $\Lambda_{i,j,k}$ can be processed by a quantizer Q, producing a reconstructed prediction error $\widehat{\Lambda}_{i,j,k}$. The associated quantized error is hereafter denoted as $\Lambda^{Q}_{i,j,k}$. Subsequent predictions $\widetilde{x}_{i,j,k}$ are calculated using reconstructed (lossy) samples $\widehat{x}_{i,j,k}$, so that the decoder can replicate this calculation and reconstruct the image samples as:

$$\widehat{x}_{i,j,k} = \widehat{\Lambda}_{i,j,k} + \widetilde{x}_{i,j,k}. \tag{2}$$

Errors in the reconstructed pixels are identical to the errors introduced by the quantizer in the prediction errors at the encoder side. That is, $x_{i,j,k} - \widehat{x}_{i,j,k} = \Lambda_{i,j,k} - \widehat{\Lambda}_{i,j,k}$. The maximum error introduced in any pixel can be precisely controlled by the quantizer step size, thus enabling near-lossless compression. A reversible mapping is then applied to the quantized prediction residual $\Lambda^{Q}_{i,j,k}$ to obtain a non-negative integer $\lambda^{Q}_{i,j,k}$. Finally, these mapped residuals can be compressed using an entropy encoder such as Golomb [33], arithmetic coding [34], or Asymmetric Numeral Systems [35].

Another key element in any compression method is allocating the available bit budget during compression to accurately achieve a target bitrate. This is a well-known problem addressed by RC techniques. The main challenge for RC when used in prediction-based coding systems is the intricate mathematical relation between the rate and the quantization applied to the prediction residuals. To solve this challenge, many RC solutions [36–41] distribute a bit budget for a collection of data elements to minimize the distortion D of the decoded image. For example, if two elements are constrained to be encoded with R_{target} bits, the optimal allocation problem is commonly formulated as:

$$\underset{Q_1,Q_2}{\operatorname{argmin}} \{D_1(Q_1) + D_2(Q_2)\} \tag{3}$$

$$\text{s.t. } R_1(Q_1) + R_2(Q_2) \leq R_{target}, \tag{4}$$

where D_e, Q_e and R_e represent the distortion, the quantization step size and the bitrate of the eth element, respectively. This formulation assumes independent quantization. In other words, the distortion and rate of the first element depends on Q_1 and not on Q_2, and vice-versa.

The problem of bit allocation given a target bitrate for a dependent quantization coding system is formulated in [38] as:

$$\underset{Q_1,Q_2}{\operatorname{argmin}} \{D_1(Q_1) + D_2(Q_1,Q_2)\} \tag{5}$$

$$\text{s.t. } R_1(Q_1) + R_2(Q_1,Q_2) \leq R_{target.} \tag{6}$$

Note that the distortion of the first element only depends on the quantization step size employed for this element, while the distortion of the second element depends on the quantization steps of both the first and the second elements.

A solution to (6) can be obtained through Lagrange multipliers by defining:

$$J_1(Q_1) = D_1(Q_1) + \lambda R_1(Q_1) \tag{7}$$

$$J_2(Q_1,Q_2) = D_2(Q_1,Q_2) + \lambda R_2(Q_1,Q_2) \tag{8}$$

and solving the following unconstrained minimization problem:

$$\underset{Q_1,Q_2}{\operatorname{argmin}} \{J_1(Q_1) + J_2(Q_1,Q_2)\}, \tag{9}$$

by adjusting λ to satisfy (6). This can be extended to more than two dependent elements in a trivial way.

Three rate control techniques have been designed for pixel-level predictive image coding systems and evaluated with the dependent predictor and entropy encoder of CCSDS 123.0-B-2 [39–41]. In [39] the input image is divided into blocks and different quantization steps are then applied to each block. The work in [40] selects a quantization step size for each color channel, instead of in a block-wise manner. Finally, [41] selects the quantization step size in a row-wise manner; i.e., it assigns the same quantization step size Q_j to each row j, across all color channels. In [41], Q_j is determined through a function that models an independent and identically distributed Laplacian source quantized by a uniform scalar quantizer. This function employs the median of medians since it is a good estimator of contiguous quantized residuals [42]. In [21,22], quantization steps are selected at the block level. It should be stressed that none of these contributions allow truly arbitrary RoIs at pixel level.

3. Proposed rate control for lossless RoI and lossy BG coding

The proposed coding system incorporates a new RC algorithm based on pixel-level prediction capable to prioritize truly arbitrary RoIs. Specifically, given a target bitrate and a RoI mask, the input image is first processed by the pixel-based predictor of CCSDS 123.0-B-2 [43]. Then, the RoI and the BG are entropy encoded with a novel context modeling that improves considerably the compression performance. The RoI is encoded losslessly and any remaining bits from the bit-budget are used to encode the BG in a lossy fashion. It is worth noting that this proposal is a one-pass method, each row j is only processed once. The proposed coding system extends the predictor and the entropy encoder of [28]. Fig. 1 displays the block diagram of the coding system, which comprises three modules: *Near-Lossless Prediction, Background Rate-control*, and *Entropy Coding*. In addition, this figure illustrates the definition of row j, as employed in this work.

A pixel-based predictor is used, which yields $\widetilde{x}_{i,j,k}$ as an estimation of pixel $x_{i,j,k}$ employing neighboring pixels. The main idea behind CCSDS 123.0-B-2 predictors is to assume spatial similarity between pixels to predict $x_{i,j,k}$. If pixels are known to be most similar to those at the same column, only the nearest pixel above the current pixel is employed. Otherwise, four spatially adjacent causal neighbours are used. Fig. 2 illustrates the spatial neighbours used to estimate $x_{i,j,k}$. However, usually, this estimation is not accurate enough to predict $x_{i,j,k}$. Therefore, the difference between the estimation and their corresponding original pixel is tracked and stored in a local difference vector. The local difference vector is further scaled with a weight vector through an inner product, which is then combined with a local sum to produce $\widetilde{x}_{i,j,k}$. In our coding system the weight vector is initialised by default as is specified in CCSDS 123.0-B-2 standard. Further details of the prediction definition and weight vector initialization can be found in [43].

Our work proposes contributions for each of the three modules comprising the coding system. In the *Near-Lossless Predictor* module, a near-lossless predictor capable of differentiating between RoI and BG is introduced. In the *Background Rate-control* module, a novel mechanism that determines the quantization step sizes to be applied to each row is introduced. The proposed RC method uses the quantized predicted BG errors $\lambda^{Q}_{i,j,k}$ to estimate the quantization step size for the next row. Quantization step sizes larger than 1 (lossy compression) are only applied to BG data, while the RoI is always losslessly encoded. Finally, in the *Entropy Encoder* module, a novel context model that generates small pieces of compressed data is introduced. This novel context model allows attaining very accurate target rates and improves considerably the lossless compression performance for the RoI. In addition, when the target bitrate is sufficiently high to compress the RoI and the BG losslessly, the coding performance for the whole image is also improved with respect to HEVC and JPEG-LS. It is worth noting that the proposed RC algorithm can be directly used with any other predictor, quantizer or entropy coder combination.

3.1. Near-lossless prediction

The simplest and most effective way to design a prediction-based lossy compression algorithm is to quantize the prediction error $\Lambda_{i,j,k}$

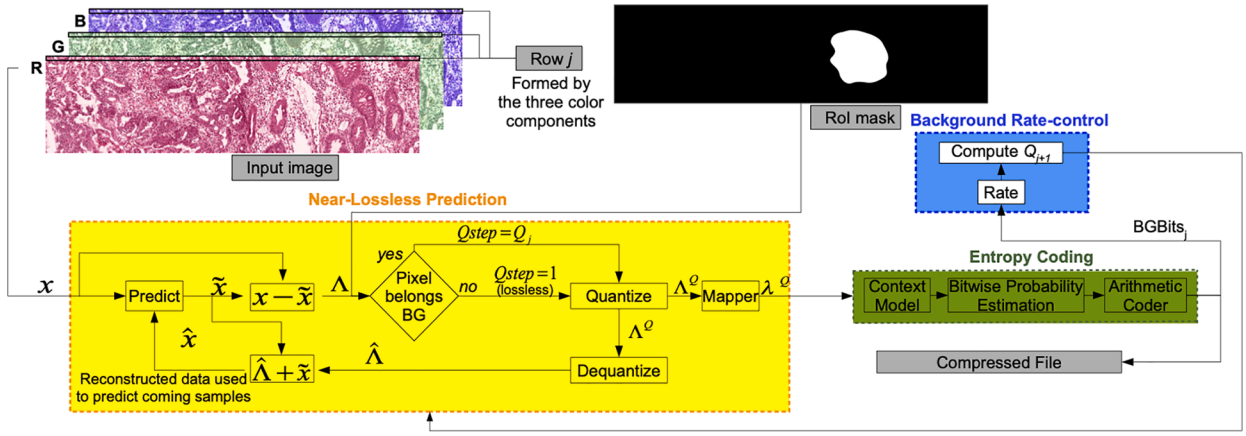

Fig. 1. Proposed RoI coding scheme with rate control for the BG area.

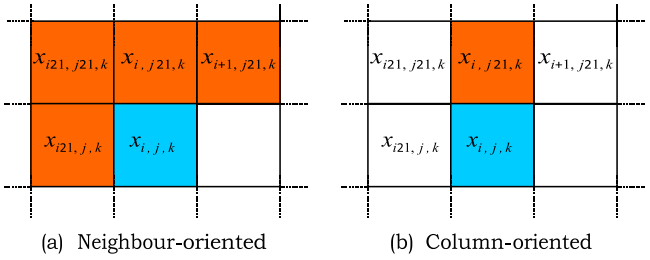

Fig. 2. Pixels used to calculate the local sum to predict $\widetilde{x}_{i,j,k}$.

with a quantizer Q, resulting in a reconstructed prediction error $\widehat{\Lambda}_{i,j,k}$ (and, in consequence, $\widehat{\lambda}_{i,j,k}$) [44]. Subsequent predictions $\widetilde{x}_{i,j,k}$ are calculated using previous reconstructed (lossy) samples $\widehat{x}_{i,j,k}$, which are obtained by reconstructing the data also at the encoder [45].

Our coding system includes a smart quantizer that discriminates between RoI, which must be encoded losslessly, and BG, which can be encoded with loss. Thus, we propose to estimate the quantization step size employed in each row j and then quantize only the BG data. The quantizer mechanism used by this method is the Uniform Scalar Deadzone Quantizer (USDQ) [11]. Note that this proposal compresses arbitrary RoIs without loss and the BG area with loss. Other techniques also encode the RoI in a lossless manner, but are restricted to define the RoI on a block-wise level, not on a pixel level [16,21,22]. Our proposed mechanism quantizes $\Lambda_{i,j,k}$, obtaining the quantized index $\Lambda^{Q}_{i,j,k}$ according to:

$$\Lambda^{Q}_{i,j,k} = \begin{cases} \text{sign}(\Lambda_{i,j,k}) \left\lfloor \dfrac{|\Lambda_{i,j,k}|}{Q_{j,k}} \right\rfloor & \text{if } x_{i,j,k} \in \text{BG} \\ \Lambda_{i,j,k} & \text{otherwise} \end{cases}, \tag{10}$$

where Q is the quantization step, with $Q \geq 1$. The operation to reconstruct $\widehat{\Lambda}_{i,j,k}$ from its quantization index is:

$$\widehat{\Lambda}_{i,j,k} = \begin{cases} \text{sign}\left(\Lambda^{Q}_{i,j,k}\right)(Q_{j,k} + \delta)\Lambda^{Q}_{i,j,k} & \text{if } x_{i,j,k} \in \text{BG} \\ \Lambda^{Q}_{i,j,k} & \text{otherwise} \end{cases}, \tag{11}$$

with $\delta = 0.5$ for $Q_{j,k} > 1$ and $\delta = 0$ for $Q_{j,k} = 1$. USDQ partitions the range of input values into several intervals, all of size $Q_{j,k}$, except for the interval that contains zero, which is of size $2Q_{j,k}$. USDQ has been selected due to its straightforward implementation and excellent performance at low bitrates [29].

3.2. Proposed background rate-control

The proposed RC method is described in Algorithm 1. This method can handle arbitrarily-shaped RoIs with pixel-level accuracy and very high target bitrate accuracy. The algorithm exploits the monotonically increasing property of $D(Q)$, i.e., $Q_1 \leq Q_2$ implies $D_1 \leq D_2$. On the other hand, the relation between Q and R is monotonically decreasing, i.e., $Q_1 \leq Q_2$ implies $R_1 \geq R_2$. Fig. 3 depicts the monotonic nature of a typical rate-distortion function.

The proposed RC method (see Algorithm 1) estimates a step size Q to be applied to the BG residual data to achieve the target-bit rate. This is obtained by applying a single quantization step size to each row j, thus only one Q value needs be stored per row as auxiliary information for decoding purposes. To attain the target bitrate, it is necessary to characterize the relation between BG residuals and step size. The proposed RC algorithm is based on four functional blocks: PREDICT($x_{i,j,k}$), QUANTIZE($\Lambda_{i,j,k}, Q^{\text{BG}}_j$, MASK), ENCODE($\lambda^{Q}_j$), and RATE($\text{BG}_k\{\}, Q^{\text{BG}}_{j+1}$).

The PREDICT($x_{i,j,k}$) function is in charge of predicting the sample $x_{i,j,k}$ and returning the prediction error $\Lambda_{i,j,k}$. Then QUANTIZE($\Lambda_{i,j,k}, Q^{\text{BG}}_j$, MASK) quantizes the associated prediction error with step size Q^{BG}_j and maps it to a positive value, returning $\lambda^{Q}_{i,j,k}$. Finally, when all the samples in a row are predicted and quantized, they are entropy coded using the ENCODE (λ^{Q}_j) function, returning the compressed bitrate BGBits$_j$ for row j in the BG.

To construct the final compressed file guaranteeing both lossless reconstruction of the RoI and accurately attaining the target bitrate, the quantization step sizes of the BG must be selected carefully. The proposed Algorithm 1 proceeds as follows:

1. Once each sample is predicted and the consequent residual is calculated (line 6 and 7), the quantizer described in Eq. (10) is employed. BG residuals are also appended to a specific list (BG{}) of the encoder to allow accurate compressed bitrate selection in successive rows of the image.
2. BGBits$_j$ is employed to compute the BG residual median of medians for estimating the rate and quantization step sizes of the coming rows (see lines 14, and 20–21).
3. After the current row is encoded, the available rate for the remaining rows is computed (lines 26–27). This is crucial to attain high RC accuracy since not all the rows have the same number of BG samples due to the arbitrary RoI shape. R_{target} is updated to denote the remaining bits, whereas rBGSamples and rBGSamples$_j$ denote, respectively, the remaining number of BG samples to be encoded and the number of BG samples in line j. Thus R^{j+1}_{target} is the BG target bitrate

Inputs: R_{target}, L, $Q^{\text{BG}} = 1$, Q^{max}

1: R=∞, rBGSamples= $\sum_{j=0}^{J-1}$ BGSamples$_j$, BG{}=$NULL$, $\widetilde{\text{BG}}${}=$NULL$
2: **for** $j = 0, ..., J-1$ **do**
3: **for** $k = 0, ..., K-1$ **do**
4: $l \leftarrow 1$
5: **for** $i = 0, ..., I-1$ **do**
6: $\tilde{x}_{i,j,k}$ = PREDICT($x_{i,j,k}$)
7: $\Lambda_{i,j,k} \leftarrow x_{j,k} - \tilde{x}_{i,j,k}$
8: $\lambda^{Q}_{i,j,k}$ = QUANTIZE($\Lambda_{i,j,k}$, Q^{BG}_j, MASK)
9: **if** $x_{i,j,k} \in$ BG **then**
10: BG.$Add(\lambda^{Q}_{i,j,k})$
11: **end if**
12: **if** i mod $L = L-1$ **then**
13: **if** $x_{i,j,k} \in$ BG **then**
14: $\widetilde{\text{BG}}$.Add(median(BG{})
15: BG{} = empty list
16: **end if**
17: **end if**
18: **end for**
19: BG$_k${} ← median($\widetilde{\text{BG}}${})
20: $\widetilde{\text{BG}}${} = empty list
21: **end for**
22: BGBits$_j \leftarrow$ ENCODE(λ^{Q}_j)
23: BGBpppc$_j$ = BGBits$_j$/BGSamples
24: $R_{\text{target}} \leftarrow R_{\text{target}}$ − BGBpppc$_j$
25: rBGSamples ← rBGSamples − BGSamples$_j$
26: $R^{j+1}_{\text{target}} \leftarrow R_{\text{target}}$/rBGSamples
27: Update R^{j+1}_{target} using (14) from [10]
28: $Q^{\text{BG}}_{j+1} \leftarrow Q^{\text{BG}}_j$
29: $R \leftarrow \sum_{k=0}^{K-1}$ RATE(BG$_k${}, Q^{BG}_{j+1})
30: **if** $R \geq R^{j+1}_{\text{target}}$ **then**
31: **while** $R \geq R^{j+1}_{\text{target}}$ AND $Q^{\text{BG}}_{j+1} < Q^{max}$ **do**
32: $R_{old} \leftarrow R$
33: $Q^{\text{BG}}_{j+1} \leftarrow Q^{\text{BG}}_{j+1} + 2$
34: $R \leftarrow \sum_{k=0}^{K-1}$ RATE(BG$_k${}, Q^{BG}_{j+1})
35: **end while**
36: **if** $|R - R^{j+1}_{\text{target}}| > |R_{old} - R^{j+1}_{\text{target}}|$ **then**
37: $Q^{\text{BG}}_{j+1} \leftarrow Q^{\text{BG}}_{j+1} - 2$
38: **end if**
39: **else**
40: **while** $R \leq R^{j+1}_{\text{target}}$ AND $Q^{\text{BG}}_{j+1} > 1$ **do**
41: $R_{old} \leftarrow R$
42: $Q^{\text{BG}}_{j+1} \leftarrow Q^{\text{BG}}_{j+1} - 2$
43: $R \leftarrow \sum_{k=0}^{K-1}$ RATE(BG$_k${}, Q^{BG}_{j+1})
44: **end while**
45: **if** $|R - R^{j+1}_{\text{target}}| > |R_{old} - R^{j+1}_{\text{target}}|$ **then**
46: $Q^{\text{BG}}_{j+1} \leftarrow Q^{\text{BG}}_{j+1} + 2$
47: **end if**
48: **end if**
49: **end for**

Algorithm 1. Proposed RC method.

for the next row to be encoded according to the remaining BG samples.

4. Assuming high similarity between adjacent rows, lines 28–29 estimate the rate R for the coming row. This estimation employs the median of medians of the BG residual data used and Q^{BG}_{j+1}, set to Q^{BG}_j —due to the high similarity assumption—, in function RATE((BG$_k${}, Q^{BG}_{j+1})). This estimation function is proposed by Valsesia in [41] using the median of all row data, whereas here only BG data is used.
5. The rest of the algorithm (lines 32–49) adapts the quantization step size for the next row to be processed Q^{BG}_{j+1}, according to the monotonically decreasing relation between Q and D.
6. The MASK is coded as auxiliary information and considered in the final rate of the generated bitstream. This ancillary data is on average about 0.003 bits per pixel per component (bpppc).

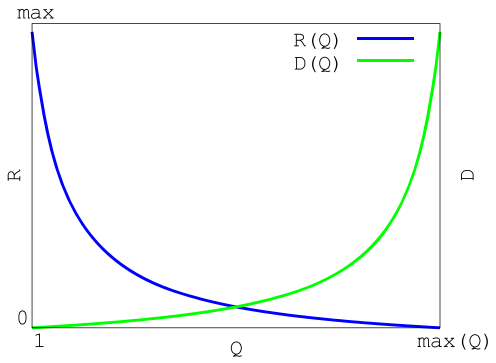

Fig. 3. Monotonicity property of a Rate-Distortion function.

3.3. Proposed entropy coding

Contextual entropy encoders employ surrounding information to estimate the probability of the symbol to be encoded with high precision; the more accurate the estimation, the better the coding performance. Once the quantized residual is obtained and mapped to a non-negative integer $\lambda^{Q}_{i,j,k}$, our proposed entropy encoder encodes $\lambda^{Q}_{i,j,k}$ with binary alphabets and a lightweight contextual arithmetic encoder [28]. This encoder employs a small context window, shown in Fig. 4(a), where the bit to be encoded is shaded in blue, and the single bit employed for the contextual modeling is the one above it, shaded in orange. Let $b^{n}_{i,j,k}$ denote the nth bit of the binary representation of $\lambda^{Q}_{i,j,k}$, with $N-1 \geq n \geq 0$. N is chosen so as to provide a sufficient number of bits to represent any possible $\lambda^{Q}_{i,j,k}$ value, with $b^{N-1}_{i,j,k}$ being the most significant bit. The entropy encoder makes use of context model patterns to encode all symbols $b^{n}_{i,j,k}$.

Consider **M** the set of all possible patterns that can occur within the context window. Context $m \in \mathbf{M}$ is then a particular realization and is associated to a unique context index $c \in \mathbf{C} = \{0,...,C-1\}$. These context indices, hereinafter simply referred to as contexts, are determined by a modeling function $F : \mathbf{M} \rightarrow \mathbf{C}$. For each bit b to be coded, a probability model is used, corresponding to its context c. In particular, our model estimates the conditional probability $p(b|c) = p(b|F(m))$. After encoding the current bit, the probability model is updated with the latest coded bit b at a context c. That is, $p(b|c)$ is estimated on the fly. Specifically, our probability model estimates the probability $p(b = 0|c)$ (and deduces probability $p(b = 1|c) = 1 - p(b = 0|c)$).

To determine the context of bit $b^{n}_{i,j,k}$, we employ a context window that contains causal bits of the current bitplane, previous bitplanes, and already encoded color channels. Neighbours used for the context modeling are depicted in Fig. 4. More specifically, Fig. 4(b) portraits the causal bit context employed for bitplane n; not-used bits in the context modeling are depicted in white. Fig. 4(c) and (e) depict bits of previous bitplanes considered for the context modeling, i.e., $n-1$ and $n-2$, when these bits have been already encoded. Fig. 4(d) and (f) show the bits employed from preceding color channels $k-1$ and $k-2$. For instance, when coding the blue channel, $k-1$ and $k-2$ refer to the green and red channels, respectively. Rather than the actual bit (from bitplane n) of each neighboring sample, the so-called "significance state"

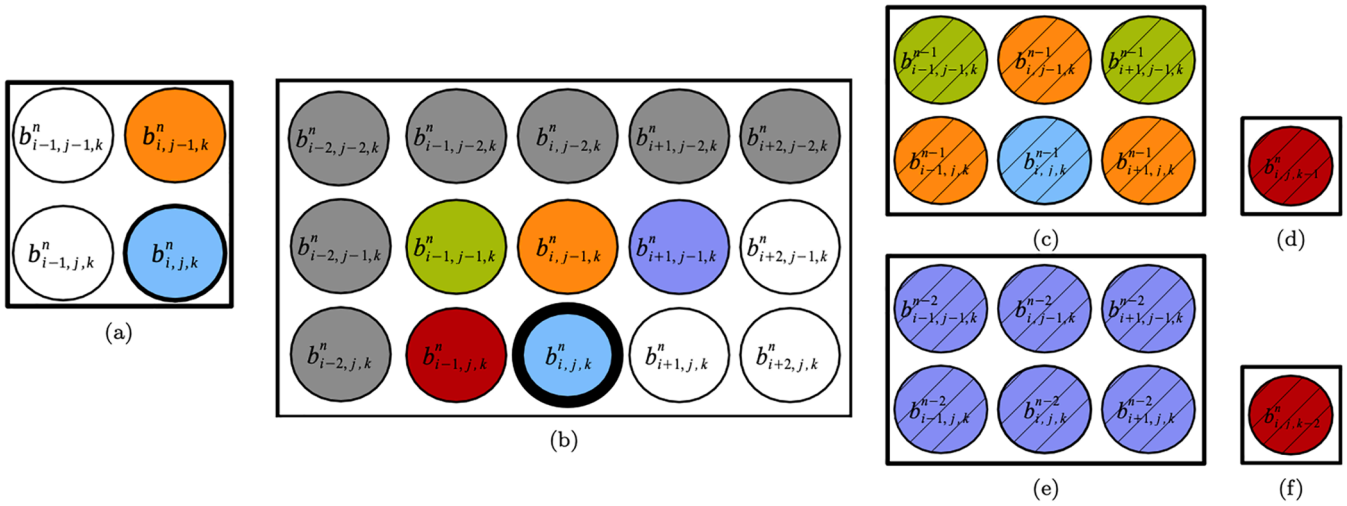

Fig. 4. Illustration of context model used to encode $b^n_{i,j,k}$. The colored bits are used as contextual data to estimate the probability. (a) Illustration of the context model selected in [28]. (b) context model bits for the current bitplane n and color channel k; (c) and (e) context model when $n < N-2$ and $n < N-3$, respectively; (d) and (f) context model when $k > 0$ and $k > 1$, respectively.

is employed to compute the context c. To this end, let $s^n_{i,j,k}$ denote the significance state of the sample at location i,j,k at bitplane n. A value of 1 indicates that the sample contains a 1 at bitplane n or higher.

Table 2 shows how c is derived from the significance states of the neighbors for a set of the causal bits represented in Fig. 4(a). This table shows the set of causal bits of Fig. 4(b) $c = [0...2^{\#t} - 1]$, where $\#t$ denotes the number of different types of neighbours evaluated. In Fig. 4(b), five different types are considered: red, green, orange, purple and gray neighbours. This is trivially extensible to a larger number of evaluated bits.

4. Experimental evaluation and discussion

This section provides results for a comprehensive set of pathology images and RoI definitions. Some of these images contain a single RoI, while others contain multiple RoIs. Seventy images for a total of more than 2 GB of data have been employed for the experimental evaluation. All images are acquired at 24 bpp with 8 bits per pixel per component (bpppc), with three components corresponding to the R, G and B color channels. They depict various tissues of different sizes and stained with Hematoxylin and Eosin (H & E) stain. In this study, a diverse set of tissues was employed for experimental analysis, encompassing: Skin fibroblast (SKNF), which synthesizes collagen and contributing to the structural integrity of the skin; Endometrial (END) to explore the cyclic changes during the menstrual cycle, mechanisms of implantation, or pathologies related to the uterus; Lung fibroblast (LNGF) employed to understanding lung diseases, fibrosis, or responses to environmental factors; Embryonic stem cells (ES), valuable in biology studies and which hold promise for regenerative medicine and cell replacement therapies; Kidney clear cell carcinoma (KIRC), for a better understanding of kidney cancer development, progression, and potential therapeutic targets; Pancreatic tissue (PANC), to cover areas such as diabetes, pancreatic cancer, or the function of pancreatic enzymes; Brain glioblastoma multiforme (GBM), which are essential for gaining insights into the biology of brain tumors; Colon adenocarcinoma (COAD), to understand colorectal cancer pathology and molecular mechanisms; and, Lymphatic (LYMP) tissues, to contribute to the understanding of immune responses, lymphatic diseases, or interactions with other organ systems. This selection represents a comprehensive range of cell types and organs, allowing for a multifaceted investigation of cellular behavior, disease processes, and potential therapeutic interventions. The inclusion of both normal and cancerous tissues underscores the study's breadth, offering insights into diverse biological phenomena and pathology.

Table 2
Context assignments considering only bits for the current bitplane n and component k, i.e., using only neighbors according to Fig. 4(b). All bits in gray have the same value in the context formation.

$s^n_{i-1,j,k}$	$s^n_{i-1,j-1,k}$	$s^n_{i,j-1,k}$	$s^n_{i+1,j-1,k}$	$s^n_{i-2,j,k}, \ldots, s^n_{i+2,j-2,k}$	c
0	0	0	0	0	0
1	0	0	0	0	1
0	1	0	0	0	2
1	1	0	0	0	3
⋮	⋮	⋮	⋮	⋮	⋮
1	1	1	1	1	31

The names, dimensions and number of RoIs of these images are tabulated in Tables 3 and 4 These images were obtained from the Center for Biomedical Informatics and Information Technology of the US National Cancer Institute [46]. To facilitate reproducibility, our implementation and the original dataset employed in our experiments are publicly available in [47] and [48], respectively. Results for reference standard software HEVC and JPEG-LS have been carried out with free available implementations [49,50]. All the experimental results are obtained in a macOS Catalina v.10.15.7 on an Intel Core i7 at 3.4 Ghz with 32 RAM GB.

The proposed coding system is evaluated using two different context models for the arithmetic encoder: either a single context bit $b^n_{i,j-1,k}$ (when available), as summarized in Section 2, hereafter referred to as *Proposed-A*; and the context modeling described in Section 3.3, hereafter referred to as *Proposed-B*. The number of color channels K is 3. In [39] it was concluded that $L = 17$ was a good election to estimate the rate of the residuals produced by the predictor of CCSDS 123.0-B-2. Thus, $L = 17$ was employed in [41,51] and also in our contribution. On the other hand, Q^{max} is the maximum quantization step applied to each line. As the bit-depth of the images in the evaluation set is of 8 bits per sample, it does not make sense to use quantization steps larger than 255. For the proposed RC method, the L and Q^{max} values are set to, respectively, 17 and 255.

To provide a meaningful comparison, Proposed-A and Proposed-B techniques are evaluated against the latest contributions [21,22]. Note that [21,22] contributions are implemented using the reference software HM16.9 of HEVC [49]. For [21,22], images are compressed using intra-prediction as a single RGB frame in 4:4:4 format, setting the largest

Table 3
Characteristics of SKNF, END, LNGF, and ES images, and absolute BRE values (in %) of all approaches. Best results are bold faced.

			[21]			[22]			Proposed-A			Proposed-B		
ID	Dimensions	#RoIs	avg	min	max	avg	min	max	avg	min	max	avg	min	max
SKNF1	3200 × 2816	5	92.903	0.001	310.658	0.945	0.079	1.344	0.208	0.000	6.337	0.005	0.001	0.072
SKNF2	4096x3328	3	74.128	0.000	281.883	0.726	0.276	0.919	0.586	0.000	17.654	0.001	0.000	0.014
SKNF3	1600x2560	1	22.558	0.025	78.589	0.695	0.222	7.981	0.740	0.000	22.213	0.000	0.000	0.008
SKNF4	1280x4160	2	7.508	0.000	92.677	0.166	0.010	0.932	0.426	0.000	12.899	0.006	0.000	0.055
SKNF5	3328x3072	2	0.012	0.001	0.078	0.051	0.003	0.329	0.007	0.001	0.172	0.001	0.000	0.016
SKNF6	4160x1280	3	0.758	0.000	16.673	0.151	0.075	0.342	0.855	0.000	25.746	0.001	0.001	0.042
SKNF7	4096x3200	4	3.773	0.003	39.542	0.346	0.014	0.581	2.353	0.000	70.537	0.000	0.000	0.016
SKNF8	1920x2880	1	52.571	0.001	493.100	0.368	0.000	4.735	2.519	0.000	70.740	0.004	0.000	0.024
SKNF9	3392x2280	4	37.846	0.002	274.435	0.197	0.015	1.059	1.858	0.000	55.709	0.002	0.000	0.020
SKNF10	2520x2880	1	69.223	0.001	230.169	0.483	0.001	4.009	1.970	0.000	58.997	0.010	0.000	0.098
All SNF images			36.128	0.000	493.100	0.413	0.000	7.981	1.151	0.000	70.740	0.001	0.000	0.098
END1	2880x3200	4	25.418	0.025	190.371	0.411	0.022	0.229	3.369	0.001	91.715	0.008	0.000	0.172
END2	3200x2816	3	26.910	0.003	211.514	0.532	0.062	1.920	0.574	0.001	17.242	0.021	0.000	0.573
END3	3072x2112	3	5.004	0.001	30.545	0.381	0.015	0.755	0.048	0.000	1.452	0.001	0.000	0.009
END4	3072x1920	2	125.714	0.006	1050.340	0.731	0.286	2.202	0.671	0.000	20.209	0.001	0.000	0.045
END5	4096x2368	1	149.344	0.002	1353.582	0.409	0.159	1.370	0.114	0.000	3.457	0.000	0.000	0.079
END6	2280x2112	2	48.888	0.003	294.768	0.289	0.059	1.370	6.051	0.000	146.312	0.001	0.001	0.145
END7	1280x4096	2	60.552	0.012	814.534	0.521	0.077	1.829	3.090	0.000	81.415	0.000	0.000	0.024
END8	2112x2816	4	9.307	0.001	133.010	0.327	0.007	1.211	1.145	0.001	34.410	0.002	0.001	0.130
END9	2816x3200	2	7.812	0.003	111.774	0.155	0.007	0.362	0.897	0.000	26.994	0.000	0.000	0.027
END10	3200x2880	1	1.971	0.000	28.569	0.279	0.087	0.754	6.304	0.001	124.887	0.025	0.000	0.557
All END images			46.092	0.000	1353.582	0.404	0.007	2.202	2.226	0.000	146.312	0.006	0.000	0.573
LNGF1	3072x3840	2	4.453	0.001	13.384	0.112	0.042	0.378	1.746	0.000	52.490	0.001	0.002	0.022
LNGF2	3840x1920	5	39.825	0.031	193.198	0.834	0.351	1.720	0.558	0.000	16.936	0.007	0.000	0.048
LNGF3	3520x2880	1	27.781	0.000	151.635	0.291	0.020	0.645	1.218	0.001	36.715	0.007	0.001	0.315
LNGF4	2816x4800	5	0.186	0.000	4.840	0.063	0.006	0.221	1.981	0.000	55.848	0.001	0.000	0.011
LNGF5	2816x2560	1	0.155	0.000	4.476	0.018	0.003	0.077	0.629	0.001	18.713	0.004	0.001	0.039
LNGF6	3392x2560	2	0.192	0.000	2.620	0.182	0.016	0.382	0.007	0.001	0.047	0.015	0.001	0.056
LNGF7	2816x2560	1	0.240	0.000	2.684	0.099	0.001	0.251	4.328	0.001	99.454	0.008	0.000	0.036
LNGF8	1600x3328	3	1.369	0.000	35.469	0.062	0.011	0.262	0.004	0.000	0.104	0.000	0.000	0.022
LNGF9	3200x3520	3	29.990	0.005	180.836	0.157	0.029	0.614	0.238	0.001	7.116	0.011	0.000	0.201
LNGF10	4096x1600	1	0.530	0.000	15.198	0.069	0.001	1.720	2.957	0.000	81.831	0.002	0.000	0.036
All LNGF images			10.472	0.000	193.198	0.189	0.001	1.720	1.366	0.000	99.454	0.003	0.000	0.315
ES1	3200x2880	2	45.602	0.002	211.894	0.555	0.115	1.153	4.150	0.000	111.816	0.005	0.000	0.070
ES2	3328x4096	3	67.626	0.004	188.937	0.600	0.008	0.870	5.764	0.000	134.976	0.001	0.001	0.019
ES3	3328x3328	3	29.127	0.001	520.424	0.823	0.190	2.387	14.069	0.000	267.493	0.002	0.000	0.052
ES4	4480x3200	6	24.751	0.000	277.427	0.643	0.001	1.180	5.508	0.000	139.455	0.001	0.000	0.040
ES5	3200x3200	1	31.364	0.001	109.611	0.501	0.079	1.601	8.045	0.000	154.633	0.001	0.001	0.052
ES6	2560x2816	4	16.288	0.000	128.471	0.508	0.006	0.989	12.018	0.001	237.043	0.012	0.002	0.418
ES7	3520x4096	5	1.208	0.000	16.403	0.070	0.004	0.292	2.359	**0.001**	70.285	0.040	0.033	**0.757**
ES8	4480x4160	2	4.381	0.000	30.130	0.111	0.045	0.404	10.410	0.000	207.878	0.016	0.001	0.277
ES9	4160x4160	5	2.007	0.000	22.876	0.104	0.005	0.355	3.235	0.000	88.601	0.015	0.001	0.249
ES10	5120x4480	3	2.651	0.000	42.384	0.054	0.010	0.222	3.519	0.001	90.679	0.025	0.000	**0.446**
All ES images			22.501	0.000	520.424	0.397	0.001	2.387	6.908	0.000	267.493	0.010	0.000	0.757

coding unit to 64 × 64 samples.

Results for four distinct approaches are then provided: [21,22], Proposed-A and Proposed-B. These results aim to assess: 1) the ability of encoding arbitrarily shaped RoIs to allow using more bits for the BG area without exceeding the target bitrate, 2) the accuracy of all the evaluated methods in terms of bitrate error (BRE), measuring how accurately the target bit rate is attained; 3) the average BRE for all tested images at a specific bitrate t, which is denoted as $\overline{\text{BRE}}_t$ and defined in Eq. (13); and 4) the impact of the proposed context modeling on the target rate accuracy and the RoI lossless coding performance.

4.1. Visual evaluation

To evaluate the visual quality of the recovered images, we show some test images reconstructed at different rates with Proposed-B and [22] in Fig. 5. The images are reconstructed at the smallest rate at which [22] losslessly recovers the RoIs. The Peak Signal-to-Noise Ratio (PSNR) of the BG is shown for each recovered image. This enables a visual evaluation of the impact of processing arbitrarily shaped RoIs and employing the remaining bits for enhancing the quality of the BG. From this visual comparison it can be appreciated that both approaches recover the RoIs without loss, but Proposed-B can also recover significant parts of the BG area, enabling a sounder clinical assessment.

4.2. Target bitrate accuracy evaluation

The BRE is defined as $\text{BRE} = |R_{\text{target}} - \text{BGBpppc}|$, which measures how precisely the target bitrate is attained. The value of BGBpppc is computed as:

$$\text{BGBpppc} = \frac{\sum_{j=0}^{J-1} \text{BGBits}_j}{\text{BGSamples}}, \tag{12}$$

where J denotes the number of rows of the image and BGSamples the number of BG samples.

The target bitrates R_{target} used to compress the image BG are $R_{\text{target}} = \{0.067, 0.134, 0.201, 0.268, 0.335, 0.402, 0.469, 0.536, 0.603, 0.67, 0.737, 0.804, 0.871, 0.938, 1.005, 1.072, 1.139, 1.206, 1.273, 1.34, 1.407, 1.474, 1.541, 1.608, 1.675, 1.742, 1.809, 1.876, 1.943, 2.000\}$, i.e., we evaluate 30 target rates per image. R_{target} is expressed in terms of

Table 4
Characteristics of KIRC, PANC, GBM, COAD, and LYMP images, and absolute BRE values (in %) of all approaches. Best results are bold faced.

			[21]			[22]			Proposed-A			Proposed-B		
ID	Dimensions	#RoIs	avg	min	max	avg	min	max	avg	min	max	avg	min	max
KIRC1	4480x3200	3	42.256	0.001	390.622	0.241	0.056	1.299	3.343	0.000	88.872	0.006	0.000	0.254
KIRC2	4160x4480	2	5.312	0.003	88.297	0.198	0.012	0.403	4.684	0.002	115.504	0.006	0.004	0.313
KIRC3	1600x3328	3	89.602	0.088	568.023	6.613	1.443	39.125	4.344	0.103	45.913	0.370	0.000	5.104
KIRC4	3520x2880	1	32.788	0.005	291.756	0.821	0.123	3.081	3.183	0.001	85.127	0.006	0.000	0.034
KIRC5	1600x1920	3	90.502	0.019	257.921	0.341	0.012	1.712	0.399	0.001	12.000	0.013	0.001	0.352
KIRC6	2816x1920	2	9.651	0.002	108.634	0.680	0.217	2.668	1.421	0.000	42.548	0.014	0.000	0.382
KIRC7	3072x2880	1	11.817	0.000	96.679	0.722	0.060	2.527	6.505	0.000	132.304	0.025	0.001	2.318
KIRC8	2560x2816	4	0.084	0.000	15.097	0.238	0.028	1.008	0.345	0.001	10.209	0.028	0.003	0.621
KIRC9	2816x4096	3	5.678	0.008	67.909	0.615	0.021	1.108	0.818	0.004	24.001	0.035	0.001	0.328
KIRC10	1280x3200	1	7.629	0.008	194.585	0.570	0.244	0.987	1.675	0.000	49.784	0.008	0.000	0.056
All KIRC images			29.532	0.000	568.023	1.104	0.012	39.125	2.672	0.000	132.304	0.031	0.000	5.104
PANC1	4800x3200	1	2.545	0.002	18.398	0.202	0.043	0.671	2.773	0.001	77.188	0.012	0.000	0.497
PANC2	1600x2560	2	0.985	0.061	17.828	1.336	0.044	4.217	4.791	0.001	114.007	0.002	0.001	0.255
PANC3	3328x3072	1	0.572	0.001	9.334	0.225	0.023	0.565	4.671	0.001	106.539	0.018	0.000	0.281
PANC4	2816x3200	3	1.269	0.001	15.001	0.086	0.001	0.479	1.660	0.000	49.852	0.010	0.000	0.363
PANC5	1920x2880	2	3.494	0.002	10.669	0.223	0.005	0.962	1.382	0.000	40.857	0.023	0.001	0.315
PANC6	2240x4096	4	11.408	**0.000**	64.197	0.221	0.036	0.968	1.021	0.001	31.025	**0.011**	0.245	0.032
PANC7	3328x3072	1	102.393	0.009	889.886	0.126	0.000	0.692	2.105	0.001	62.866	0.012	0.000	0.118
PANC8	3520x2560	3	0.535	0.000	6.980	0.056	0.001	0.439	1.927	0.000	58.021	0.001	0.001	0.080
PANC9	2112x2816	1	1.114	0.001	11.215	0.077	0.000	0.396	1.280	**0.000**	37.696	0.045	0.004	0.229
PANC10	3072x2816	1	0.448	0.003	9.228	0.037	**0.000**	0.306	0.018	0.004	1.015	0.003	0.002	0.199
All PANC images			12.476	0.000	889.886	0.259	0.000	4.217	2.163	0.000	114.007	0.011	0.000	0.497
GBM1	4480x3840	3	6.675	0.016	42.022	0.264	0.142	1.456	2.041	0.000	57.264	0.000	0.000	0.046
GBM2	3392x3072	1	19.984	0.000	137.293	0.015	0.000	0.074	4.475	0.000	96.940	0.014	0.000	0.275
GBM3	3520x2880	2	110.748	1.963	427.996	0.724	0.383	2.054	2.742	0.000	71.825	0.003	0.000	0.016
GBM4	2880x2816	4	0.390	0.000	5.800	0.129	0.010	0.647	1.722	0.001	51.773	0.005	0.000	0.029
All GBM images			34.449	0.000	427.996	0.283	0.000	2.054	2.745	0.000	96.940	0.004	0.000	0.275
COAD1	4096x3840	2	41.423	0.000	177.730	0.154	0.041	0.687	1.619	0.001	48.848	0.004	0.000	0.049
COAD2	2816x4480	3	1.936	0.001	9.374	1.611	0.089	4.712	5.920	0.128	86.699	0.520	0.000	**5.745**
COAD3	3840x3200	2	2.572	0.000	15.572	0.093	0.007	0.840	3.146	0.000	79.525	0.005	0.000	0.027
All COAD images			15.310	0.000	177.730	0.619	0.007	4.712	3.562	0.000	86.699	0.173	0.000	19.783
LYMP1	1280x1280	1	9.374	0.004	87.621	0.673	0.281	5.630	9.246	0.001	203.276	0.007	0.000	0.046
LYMP2	1920x3840	2	0.128	0.001	1.322	0.166	0.009	0.571	4.376	0.000	112.342	0.015	0.000	0.054
LYMP3	4480x4480	3	19.990	0.000	162.425	0.361	0.020	2.293	4.080	0.001	99.354	0.014	0.000	1.073
All LYMP images			9.831	0.000	162.425	0.400	0.009	5.630	5.901	0.000	203.276	0.002	0.000	1.073
All images in Table 3 and 4			25.503	0.000	1353.582	0.455	0.000	39.125	2.917	0.000	267.493	0.008	0.000	**5.745**

bpppc.

Tables 3 and 4 show the average absolute BRE values for all target bitrates, along with the minimum and maximum BRE values achieved for each image by all evaluated approaches. These results are labeled as "avg", "min", and "max", respectively. The BRE is provided in percentage with respect to the target bitrate, computed as $100 \cdot \text{BRE} \ / R_{\text{target}}$. Reported results are grouped by tissue type. The last row of Table 4 displays results for all the tested images.

From these results, it can be seen that Proposed-B yields better performance in terms of BRE than Proposed-A and [22] on average for all images. It is worth noting that the maximum BRE values for [22], Proposed-A, and -B are, respectively, 39.125%, 267.493% and 5.745%, clearly showing the better performance of our Proposed-B approach. In turn, [22] yields better results than Proposed-A in terms of average BRE. Proposed-B outperforms the latest contribution [22] for all tissue types and aggregation functions (minimum, maximum and average), except for only 4 images and always for the case of the minimum BRE value.

Our RC algorithm produces consistent performance for all tissue types. More concretely, the average BRE attained by our algorithm for all evaluated images is 0.008%, i.e., 56.87 times smaller compared to the 0.455% of [22]. Furthermore, it produces minimum and maximum BRE values closer to zero than [22].

Fig. 6 plots BRE results for [21,22] and Proposed-B for each target bpppc, for SKNF6, END1, LNGF1, and PANC5 images. The horizontal and vertical axes denote the target bpppc and the BRE expressed as a percentage of the target bpppc, respectively. Note that our proposal attains BRE values closer to 0 (higher accuracy) than [21,22] for all bitrates (except at the extremely low rate 0.067 bpppc for LNGF1 and PANC5 images). Moreover, Proposed-B is very stable in terms of bitrate accuracy for all the assessed rates.

Finally, Fig. 7 plots the average BRE for all tested images at a specific bitrate $t \in R_{\text{target}}$, which is referred to as $\overline{\text{BRE}}_t$, and is computed as:

$$\overline{\text{BRE}}_t = \frac{1}{M}\left(\sum_{m=0}^{M-1} \left| R_{\text{target}_t} - \text{BGBpppc}_t \right| \right), \tag{13}$$

where M denotes the number of tested images.

$\overline{\text{BRE}}_t$ is plotted for Proposed-B and for [22]. From this plot, it can be seen that Proposed-B attains the lowest $\overline{\text{BRE}}_t$ values for all target bitrates. For both methods, the largest $\overline{\text{BRE}}_t$ values are provided at very low bitrates. This is due to the small degree of freedom when distributing the available budget across the whole image. In turn, the lowest values of $\overline{\text{BRE}}_t$ are obtained in the middle range of R_{target}, i.e., $0.800 \leq R_{\text{target}_t} \leq 1.600$. Our proposal achieves better results than [22], always producing $\overline{\text{BRE}}_t < 0.2\%$, except for the target bitrate 0.133 bpppc, for which $\overline{\text{BRE}}_t = 0.39\%$.

4.3. Lossless compression performance

This experiment is aimed to evaluate lossless compression

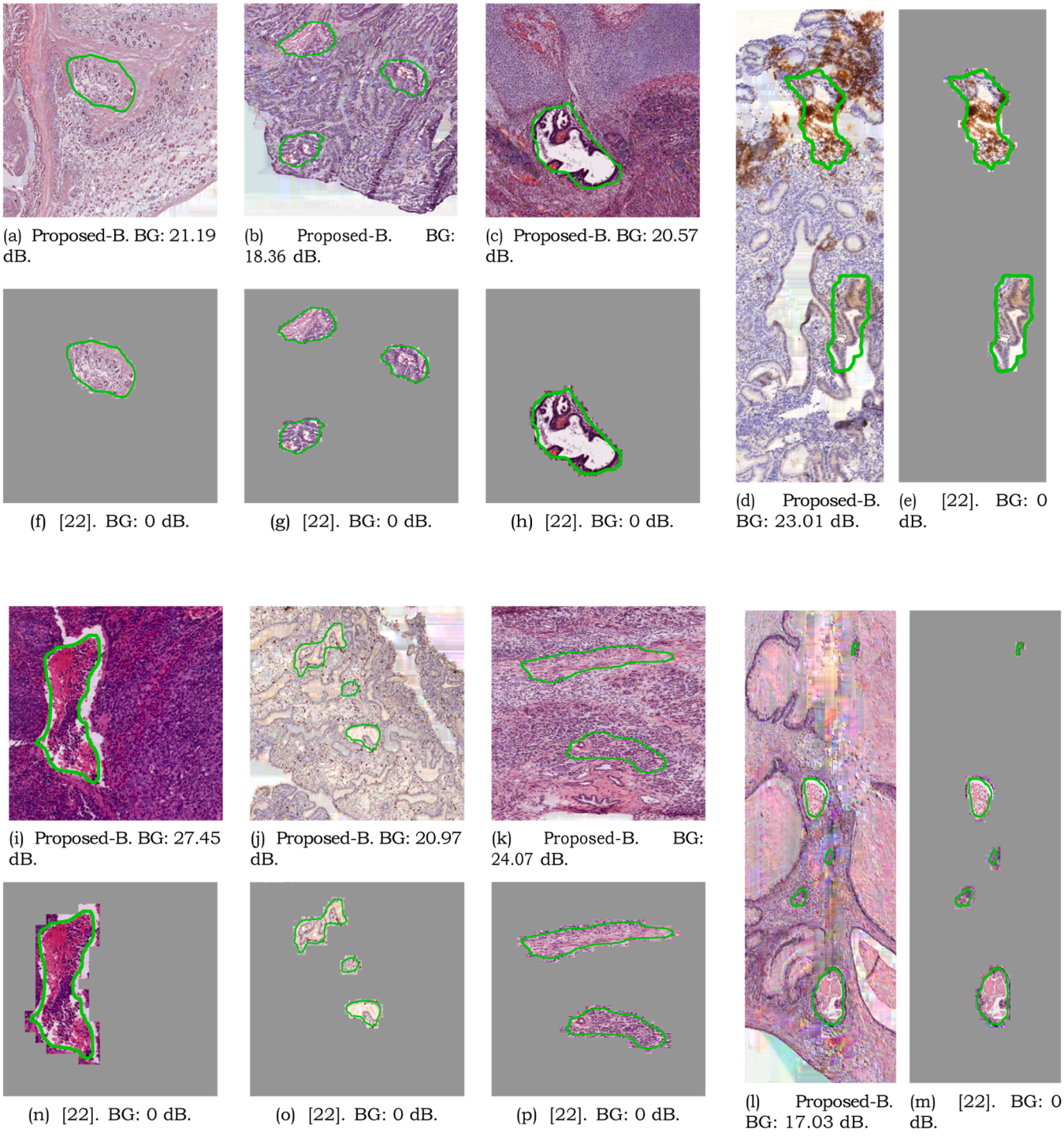

Fig. 5. Visual comparison of recovered images with Proposed-B and [22] for different images. (a) and (f) SKIN10 at 0.5 bpppc, (b) and (g) END7 at 0.5 bpppc, (c) and (h) COAD2 at 0.5 bpppc, (d) and (e) LNGF7 at 0.5 bpppc, (i) and (n) LYMP1 at 1 bpppc, (j) and (o) END2 at 0.3 bpppc, (k) and (p) PANC2 at 0.75 bpppc, and (l) and (m) LNGF2 at 0.3 bpppc. All RoIs, green delimited, are losslessly recovered for both evaluated methods.

performance for the RoI and for the entire image. Columns 2–5 of Table 5 shows the lossless compression performance of HEVC, JPEG-LS, Proposed-A and Proposed-B for the entire images (RoI + BG). Columns 7 and 8 indicate the amount of samples belonging to the RoI used by Sanchez et al. [21], Sanchez and Hernández-Cabronero [22] and our proposals. Note that the number of RoI samples used by Sanchez et al. [21], Sanchez and Hernández-Cabronero [22] is larger because RoIs are defined on a block level, as opposed to our pixel-level approach. Finally, column with symbol ★ provides the lossless coding performance for only the RoI area when using [21,22]. Columns with symbol ✤ and ✦ provide the lossless coding performance for RoI areas for the Proposed-A and Proposed-B methods, as well as the percentage difference with respect to column ★. For Proposed-A and Proposed-B, the percentage gain compared to [21,22] is also reported. It is worth noting that, considering that the size of the dataset is about 2GB, and that the RoI compression performance is, on average, 0.44 for [21,22] and 0.31 for our proposal, the lossless storage or transmission of all the RoIs would need 112MB for [21,22] and 79MB for our proposal.

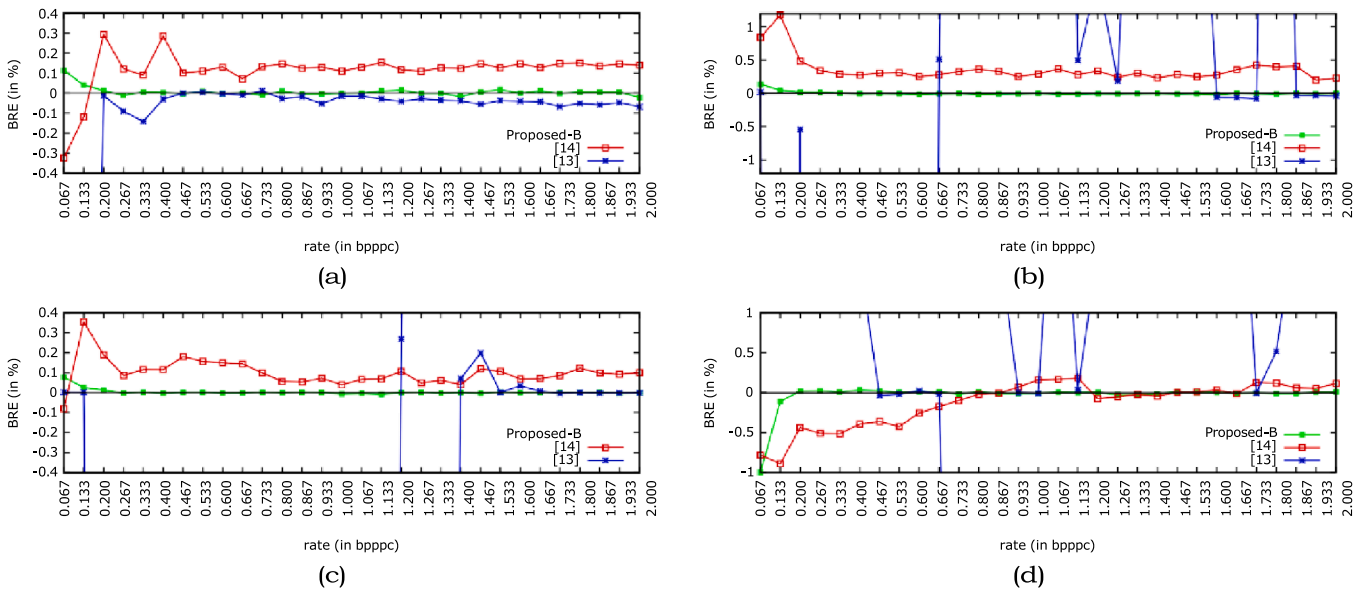

Fig. 6. Average BRE values (in %) of the evaluated approaches for 30 bitrates (bpppc). (a) SKNF6, (b) END1, (c) LNGF1, and (d) PANC5.

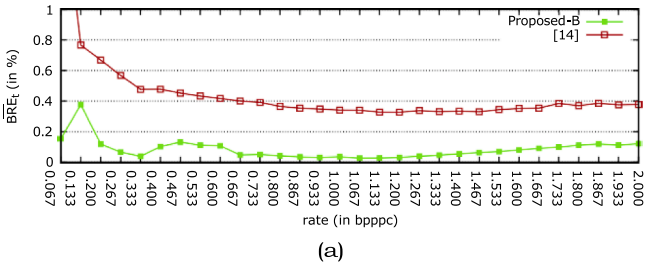

Fig. 7. $\overline{\mathrm{BRE}}_t$ (in %) averaged for all the images for the Proposed-B and [22].

The lossless compression results indicate that, on average and for all tissues, Proposed-A and Proposed-B outperform HEVC. This also occurs for JPEG-LS, with the exception of SKNF3. Compared to HEVC and JPEG-LS, Proposed-B provides an improvement in compression performance, on average for all tissues, of 13.61% and 15.06%, respectively. Proposed-A and Proposed-B outperform [21,22] for the case of lossless compression of the RoI only, furthermore Proposed-B provides much better performance than Proposed-A. On average, improvements close to 16% and 30% compared to [21,22] are observed for Proposed-A and Proposed-B, respectively.

4.4. Execution time evaluation

The last results are aimed at assessing the coding time of the proposal when performing lossless compression. Table 6 provides the lossless compression times for Proposed-A, Proposed-B, HEVC, and JPEG-LS. Execution time is measured as the total user and system time reported by the operating system. All experiments have been executed on a single thread. The HEVC and JPEG-LS implementations used are freely available at [49,50]. It is worth noting that [21] and [22] use the HEVC implementation evaluated here as their baseline. The fastest implementation of all tested compressors is JPEG-LS, however it provides the poorest lossless compression performance. The slowest compressor is HEVC, which is almost 44 and 17 times slower than Proposed-A and Proposed-B, respectively. It can be observed that Proposed-B is, approximately, 2.7 times slower than Proposed-A.

The computational complexity of the proposed approach can be determined by enumerating the operations per sample executed during the encoding procedure by the different functions. Let $n = J{\cdot}K{\cdot}I$ represent the total number of samples to be compressed. Then, considering that the inner loop entails invocations of the Predict and Quantize functions, denoted, respectively, as $f(n)$ and $g(n)$ and which are linear with respect of n, and that the list operations exhibit a complexity of $O(n)$ in the worst-case scenario, the overall complexity can be succinctly expressed as $O(f(n) + g(n)) = O(n)$.

4.5. Discussion

According to the visual comparison, Proposed-B can also recover significant parts of the BG area because our coding system only encodes losslessly those pixels that are marked as RoI. Hence, more bits can be assigned to the background area while meeting the target bitrate. According to the physicians who coauthor this paper, the BG area recovered at low bitrates provides biological contextual information, thus enabling a sounder clinical diagnosis than all previously proposed methods at same bitrates.

In terms of target bitrate accuracy, Proposed-B yields better results than Proposed-A and [22] because Proposed-B employs a sophisticated probability estimator with more contextual information —including current and previous bitplanes and processed color channels—. This is because the adaptive context model generates smaller bitstream portions per processed row, which allows meeting the target bitrate more accurately than Proposed-A and [21,22]. It is important to note that the difference in max values are very large because at very-low rates the context model cannot generate bitstreams small enough to attain the target bitrate.

Regarding the lossless compression performance of the whole Image and the RoI, Proposed-B outperforms HEVC and JPEG-LS when the whole image or RoI are losslessly encoded. These improvements are due to the ability of our coding system to employ the predictor of CCSDS 123.0-B-2 followed by a binary entropy encoder that relies on a sophisticated new context modeling defined in Section 3.3; this modeling allows accurate probabilities estimation. It is worth noting that the lossless compression bitrate is 4.70 and 4.06 bpppc on average for HEVC (the base coding technique of [21,22]) and our proposal, respectively. Therefore, the 2 GB test corpus can be losslessly compressed using 1.17 GB and 1.01 GB, respectively.

Based on the obtained execution times, Proposed-B is 2.7 times slower than Proposed-A. This can be explained by the larger amount of computations executed during the context modeling procedure. While Proposed-A only checks one neighbor of the current bit, Proposed-B

Table 5
Lossless and RoI lossless compression performance (in bpppc) results for SKNF, END, LNGF, KIRC, PANC, GBM, COAD and LYMP images.

	Whole Image Lossless Compression				RoI Lossless Compression								
							[21,22]	Proposed	★	✤		✦	
ID	Entropy	HEVC	JPEG-LS	Proposed-A	Proposed-B	#RoIs	#RoI samples x1000	#RoI samples x1000	[21,22]	Proposed-A		Proposed-B	
SKNF1	7.57	5.63	5.22	5.22	**5.09**	5	303.10	200.64	0.20	0.19	4.35 %	0.13	34.55 %
SKNF2	7.17	5.02	4.76	4.71	**4.49**	3	573.44	418.76	0.25	0.26	-2.81 %	0.19	24.87 %
SKNF3	7.11	5.20	**4.53**	4.80	4.62	1	126.98	88.06	0.18	0.15	17.13 %	0.12	33.71 %
Avg SKNF	6.17	5.53	4.84	5.08	**4.73**	-	334.51	235.82	0.21	0.20	6.22 %	0.15	31.04 %
END1	7.27	4.52	4.64	4.18	**4.02**	4	1187.84	921.87	0.57	0.47	18.26 %	0.40	34.55 %
END2	7.16	4.34	4.78	4.03	**3.84**	3	540.67	379.54	0.30	0.25	16.85 %	0.20	24.87 %
END3	7.31	5.18	4.96	4.88	**4.71**	3	307.20	213.28	0.27	0.19	30.51 %	0.14	33.71 %
Avg END	7.24	4.68	4.79	4.36	**4.19**	-	678.57	504.90	0.38	0.30	21.87 %	0.25	31.04 %
LNGF1	7.61	5.15	4.82	4.55	**4.44**	2	765.95	622.72	0.35	0.34	18.70 %	0.27	30.43 %
LNGF2	7.44	5.01	4.84	4.59	**4.41**	5	372.74	238.40	0.27	0.21	36.04 %	0.16	33.48 %
LNGF3	6.92	4.87	4.34	4.41	**4.26**	1	606.21	435.46	0.33	0.30	28.17 %	0.23	48.80 %
Avg LNGF	7.32	5.01	4.66	4.52	**4.37**	-	581.63	432.19	0.31	0.28	27.64 %	0.22	37.57 %
KIRC1	7.63	4.78	4.50	4.39	**4.08**	3	1597.44	1007.20	0.48	0.44	8.89 %	0.35	27.53 %
KIRC2	7.77	4.47	5.18	3.94	**3.62**	2	2326.53	2040.94	0.59	0.54	8.03 %	0.46	21.65 %
KIRC3	7.06	3.81	4.26	3.46	**3.16**	3	851.97	129.62	0.22	0.13	40.59 %	0.11	49.73 %
Avg KIRC	7.49	4.35	4.65	3.93	**3.62**	-	1591.98	1059.25	0.43	0.37	19.17 %	0.31	32.97 %
PANC1	7.78	4.65	5.00	4.10	**3.92**	1	1179.65	1034.15	0.39	0.39	0.00 %	0.32	17.95 %
PANC2	7.55	5.01	4.73	4.36	**4.24**	2	602.11	436.65	0.76	0.56	26.56 %	0.50	34.43 %
PANC3	7.11	3.36	4.14	3.22	**3.07**	1	1687.55	1490.30	0.70	0.53	24.38 %	0.51	27.23 %
Avg PANC	7.48	4.34	4.62	3.89	**3.74**	-	1156.44	987.03	0.62	0.49	16.98 %	0.44	26.54 %
GBM1	7.64	4.49	4.90	4.05	**3.81**	3	1306.62	1039.69	0.36	0.31	12.92 %	0.26	26.97 %
GBM2	7.19	4.46	4.45	3.96	**3.82**	1	921.60	780.43	0.47	0.37	22.08 %	0.32	32.61 %
GBM3	7.13	4.85	4.92	4.53	**4.22**	2	782.34	636.89	0.40	0.39	1.71 %	0.31	21.87 %
Avg GBM	7.32	4.60	4.75	4.18	**3.95**	-	1003.52	819.00	0.41	0.36	12.24 %	0.30	27.15 %
COAD1	7.65	5.01	5.03	4.38	**4.24**	2	1019.90	850.43	0.33	0.33	0.63 %	0.27	18.70 %
COAD2	7.18	4.35	5.10	4.06	**3.74**	3	1150.98	927.93	0.48	0.47	1.92 %	0.38	20.70 %
COAD3	7.61	4.90	5.21	4.49	**4.30**	2	925.70	736.89	0.39	0.37	5.43 %	0.30	23.32 %
Avg COAD	7.48	4.75	5.11	4.31	**4.09**	-	1032.19	838.42	0.40	0.39	2.66 %	0.32	20.91 %
LYMP1	7.74	4.70	4.75	4.12	**3.94**	1	299.01	205.48	0.97	0.76	21.99 %	0.62	36.36 %
LYMP2	7.55	4.39	4.48	3.70	**3.45**	2	1052.67	850.80	0.68	0.52	23.44 %	0.44	35.22 %
LYMP3	7.23	4.00	4.96	3.64	**3.36**	3	2125.82	1827.04	0.55	0.49	10.65 %	0.41	25.24 %
Avg LYMP	7.51	4.36	4.73	3.82	**3.58**	-	1159.17	961.11	0.73	0.59	18.70 %	0.49	32.27 %
Avg	7.25	4.70	4.78	4.26	**4.06**	-	942.25	729.71	0.44	0.37	15.68%	0.31	29.94%

evaluates 25 neighbors (see Fig. 4). Overall, Proposed-B provides a very good trade-off between coding performance and coding time.

5. Conclusions

This paper introduces a coding system based on prediction that includes a novel Rate Control (RC) algorithm for Region of Interest (RoI) coding in pathology imaging and employs a novel smart context modeling for entropy encoding. The proposed RC method selects and carefully controls the quantization step sizes applied to the BG to accurately achieve a target bitrate. Residual data produced by the predictor are entropy coded using a lightweight arithmetic encoder with a new smart context modeling. The new context model allows to efficiently construct small sets of bitstreams. The proposed RC approach is compared to other RC algorithms designed to encode RoIs without any loss and the BG with losses. Results over a large set of pathology images with multiple RoIs suggest that the proposed coding system attains the target bitrate for the BG much more precisely than other state-of-the-art methods. The bitrate error reduction is in the order of 56 times smaller on average. Furthermore, the proposed system is also able to produce smaller compressed bit streams when compressing the RoI in a lossless regime, allowing to transmit more contextual background data. In addition, our proposed coding system outperforms the best-performing lossless compression methods included in DICOM, HEVC and JPEG-LS standards, when the whole image (RoI + BG) is compressed in a lossless manner, achieving average bitrate reductions of 15.7% and 17.7%, respectively. Our proposal recovers more BG information, allowing the pathologists to have more contextual information for the clinical diagnosis.

CRediT authorship contribution statement

Joan Bartrina-Rapesta: Conceptualization, Funding acquisition, Investigation, Methodology, Resources, Software, Supervision, Validation, Visualization, Writing – original draft, Writing – review & editing. **Miguel Hernández-Cabronero:** Software, Supervision, Writing – original draft, Writing – review & editing. **Victor Sanchez:** Methodology, Writing – original draft, Writing – review & editing. **Joan Serra-Sagristà:** Formal analysis, Funding acquisition, Methodology, Writing – original draft, Writing – review & editing. **Pouya Jamshidi:** Formal analysis, Validation. **J. Castellani:** Formal analysis, Validation.

Declaration of competing interest

The authors declare that they have no known competing financial interests or personal relationships that could have appeared to influence

Table 6
Lossless coding times for HEVC, JPEG-LS, Proposed-A and Proposed-B for SKNF, END, LNGF, KIRC, PANC, GBM, COAD and LYMP images.

	Coding time (in seconds)			
ID	HEVC	JPEG-LS	Proposed-A	Proposed-B
SKNF1	2402.5	4.8	52.0	149.8
SKNF2	3628.2	7.0	77.3	218.4
SKNF3	1078.3	2.2	24.2	73.2
Average SKNF	2369.6	4.7	51.2	147.1
END1	2363.1	4.6	52.9	142.4
END2	2319.9	4.6	51.2	136.5
END3	2219.0	4.6	49.8	137.1
Average END	2300.6	4.6	51.3	138.6
LNGF1	3250.3	6.0	67.4	181.4
LNGF2	2028.0	3.8	43.4	118.1
LNGF3	2748.7	5.0	57.7	158.5
Average LNGF	2675.7	4.9	56.2	152.6
KIRC1	3953.0	7.2	80.0	218.0
KIRC2	5131.0	9.9	101.7	268.5
KIRC3	1406.9	2.5	30.3	82.6
Average KIRC	3497.0	6.5	70.7	189.7
PANC1	4227.2	7.9	87.5	223.3
PANC2	1103.1	2.1	24.0	70.5
PANC3	2664.1	4.9	57.8	154.3
Average PANC	2664.8	4.9	56.4	149.4
GBM1	4600.2	9.2	98.4	249.3
GBM2	2750.2	5.1	59.9	157.4
GBM3	2666.5	5.2	62.2	152.5
Average GBM	3339.0	6.5	73.5	186.4
COAD1	4269.1	8.0	89.2	243.6
COAD2	3177.5	6.6	71.2	185.6
COAD3	3257.4	6.5	68.3	189.1
Average COAD	3568.0	7.0	76.2	206.1
LYMP1	450.2	0.9	11.9	33.6
LYMP2	1976.2	3.7	42.4	110.2
LYMP3	5227.8	10.3	112.5	281.6
Average LYMP	2551.4	5.0	55.6	141.8
Average	2870.8	5.5	61.4	164.0

the work reported in this paper.

Data availability

We have shared the link as a reference in the article

References

[1] K. Bera, K.A. Schalper, D.L. Rimm, V. Velcheti, A. Madabhushi, Artificial intelligence in digital pathology —new tools for diagnosis and precision oncology, Nat. Rev. Clin. Oncol. 16 (11) (2019) 703–715, https://doi.org/10.1038/s41571-019-0252-y.

[2] M.S. Hosseini, J.A.Z. Brawley-Hayes, Y. Zhang, L. Chan, K.N. Plataniotis, S. Damaskinos, Focus quality assessment of high-throughput whole slide imaging in digital pathology, IEEE Trans. Med. Imaging 39 (1) (2020) 62–74, https://doi.org/10.1109/TMI.2019.2919722.

[3] B.-R. Wei, C.H. Halsey, S.B. Hoover, M. Puri, H.H. Yang, B.D. Gallas, M.P. Lee, W. Chen, A.C. Durham, J.E. Dwyer, M.D. Sánchez, R.P. Traslavina, C. Frank, C. Bradley, L.D. McGill, D.G. Esplin, P.A. Schaffer, S.D. Cramer, L.T. Lyle, J. Beck, E. Buza, Q. Gong, S.M. Hewitt, R.M. Simpson, Agreement in histological assessment of mitotic activity between microscopy and digital whole slide images informs conversion for clinical diagnosis, Acad. Pathol. 6 (2019), https://doi.org/10.1177/2374289519859841.2374289519859841

[4] C. Bernard, S. Chandrakanth, I. Cornell, J. Dalton, A. Evans, B. Garcia, C. Godin, M. Godlewski, G. Jansen, A. Kabani, S. Louahlia, L. Manning, R. Maung, L. Moore, J. Philley, J. Slatnik, J. Srigley, A. Thibault, D. Picard, H. Cracower, B. Tetu, Guidelines from the Canadian Association of Pathologists for establishing a telepathology service for anatomic pathology using whole-slide imaging, J. Pathol. Inf. 5 (1) (2014) 15, https://doi.org/10.4103/2153-3539.129455.

[5] D. Racoceanu, D. Ameisen, A. Veillard, B.B. Cheikh, E. Attieh, P. Brezillon, J.-B. Yunés, J.-M. Temerson, L. Toubiana, V. Verger, J.-F. Pomerol, J. Klossa, F. Lallemand, P. Constant, F. Capron, C. Guettier, N. Phan, P. Bertheau, Towards efficient collaborative digital pathology: a pioneer initiative of the flexmim project, Diagn. Pathol. 1 (8) (2016).

[6] M. Sahota, B. Leung, S. Dowdell, et al, Learning pathology using collaborative vs. individual annotation of whole slide images: a mixed methods trial, BMC Med. Edu. 16 (5) (2016) 311, https://doi.org/10.1186/s12909-016-0831-x.

[7] T.S. King, R. Sharma, J. Jackson, K.R. Fiebelkorn, Clinical case-based image portfolios in medical histopathology, Anat. Sci. Educ. 12 (2) (2019) 200–209, https://doi.org/10.1002/ase.1794.

[8] S. Nauhria, L. Hangfu, Virtual microscopy enhances the reliability and validity in histopathology curriculum: practical guidelines, MedEdPublish 8 (1) (2019), https://doi.org/10.15694/mep.2019.000028.2.

[9] T. Song, V. Sanchez, H. EIDaly, N.M. Rajpoot, Dual-channel active contour model for megakaryocytic cell segmentation in bone marrow trephine histology images, IEEE Trans. Biomed. Eng. 64 (12) (2017) 2913–2923, https://doi.org/10.1109/TBME.2017.2690863.

[10] Digital Image and Communication in Medicine, DICOM, 2023, https://www.dicomstandard.org/.

[11] D.S. Taubman, M.W. Marcellin, JPEG2000 Image Compression Fundamentals, Standards and Practice, Kluwer Academic Publishers, Norwell, Massachusetts 02061 USA.

[12] H.264 - advanced video coding for generic audiovisual services, 2003.

[13] G.J. Sullivan, J. Ohm, W. Han, T. Wiegand, Overview of the High Efficiency Video Coding (HEVC) standard, IEEE Trans. Circuits Syst. Video Technol. 22 (12) (2012) 1649–1668.

[14] H.265 - high efficiency video coding, 2013.

[15] V. Sanchez, F. Aulílinás, J. Bartrina-Rapesta, J. Serra-Sagrist', HEVC-based lossless compression of whole slide pathology images. IEEE Global Conference on Signal and Information Processing, 2014, pp. 297–301, https://doi.org/10.1109/GlobalSIP.2014.7032126.

[16] H. Chen, G. Braeckman, S.M. Satti, P. Schelkens, A. Munteanu, HEVC-based video coding with lossless region of interest for telemedicine applications. 20th International Conference on Systems, Signals and Image Processing, 2013, pp. 129–132, https://doi.org/10.1109/IWSSIP.2013.6623470.

[17] V. Sanchez, F.A. Llinás, J.B. Rapesta, J.S. Sagristá, Improvements to HEVC intra coding for lossless medical image compression. 2014 Data Compression Conference, 2014, https://doi.org/10.1109/DCC.2014.76.pp. 423–423

[18] Y. Liu, Z.G. Li, Y.C. Soh, Region-of-interest based resource allocation for conversational video communication of H.264/AVC, IEEE Trans. Circuits Syst. Video Technol. 18 (1) (2008) 134–139, https://doi.org/10.1109/TCSVT.2007.913754.

[19] M. Meddeb, M. Cagnazzo, B. Pesquet-Popescu, Region-of-interest-based rate control scheme for high-efficiency video coding, APSIPA Trans. Signal Inf. Process. 3 (2014) e16, https://doi.org/10.1017/ATSIP.2014.15.

[20] M. Xu, X. Deng, S. Li, Z. Wang, Region-of-interest based conversational HEVC coding with hierarchical perception model of face, IEEE J. Sel. Top. Signal Process. 8 (3) (2014) 475–489, https://doi.org/10.1109/JSTSP.2014.2314864.

[21] V. Sanchez, F. AulíLlinás, R. Vanam, J. Bartrina-Rapesta, Rate control for lossless region of interest coding in HEVC intra-coding with applications to digital pathology images. IEEE International Conference on Acoustics, Speech and Signal Processing, 2015, pp. 1250–1254, https://doi.org/10.1109/ICASSP.2015.7178170.

[22] V. Sanchez, M. Hernández-Cabronero, Graph-based rate control in pathology imaging with lossless region of interest coding, IEEE Trans. Med. Imaging 37 (10) (2018) 2211–2223, https://doi.org/10.1109/TMI.2018.2824819.

[23] J. El Sayeh Khalil, A. Munteanu, P. Lambert, Scalable wavelet-based coding of irregular meshes with interactive region-of-interest support, IEEE Trans. Circuits Syst. Video Technol. 29 (7) (2019) 2067–2081, https://doi.org/10.1109/TCSVT.2018.2860525.

[24] M. Zhou, X. Wei, S. Wang, S. Kwong, C.-K. Fong, P.H.W. Wong, W.Y.F. Yuen, Global rate-distortion optimization-based rate control for HEVC HDR coding, IEEE Trans. Circuits Syst. Video Technol. 30 (12) (2020) 4648–4662, https://doi.org/10.1109/TCSVT.2019.2959807.

[25] V. Sanchez, Rate control for predictive transform screen content video coding based on RANSAC, IEEE Trans. Circuits Syst. Video Technol. 31 (11) (2021) 4422–4438, https://doi.org/10.1109/TCSVT.2020.3047296.

[26] Z. Liu, X. Pan, Y. Li, Z. Chen, A game theory based CTU-level bit allocation scheme for HEVC region of interest coding, IEEE Trans. Image Process. 30 (2021) 794–805, https://doi.org/10.1109/TIP.2020.3038515.

[27] Y. Jiang, R. Cui, F. Liu, Multi-resolutional human visual perception optimized pathology image progressive coding based on JPEG2000, Signal Process. Image Commun. 115 (2023) 116960, https://doi.org/10.1016/j.image.2023.116960.

[28] J. Bartrina-Rapesta, I. Blanes, F. AulíLlinás, J. Serra-Sagristá, V. Sanchez, M. W. Marcellin, A lightweight contextual arithmetic coder for on-board remote sensing data compression, IEEE Trans. Geosci. Remote Sens. 55 (8) (2017) 4825–4835, https://doi.org/10.1109/TGRS.2017.2701837.

[29] Information technology - JPEG 2000 image coding system - Part 1: core coding system, 2000.

[30] L.F.R. Lucas, N.M.M. Rodrigues, L.A. da Silva Cruz, S.M.M. de Faria, Lossless compression of medical images using 3-D predictors, IEEE Trans. Med. Imaging 36 (11) (2017) 2250–2260, https://doi.org/10.1109/TMI.2017.2714640.

[31] F. Liu, M. Hernández-Cabronero, V. Sanchez, M.W. Marcellin, A. Bilgin, The current role of image compression standards in medical imaging, Information 8 (4) (2017), https://doi.org/10.3390/info8040131.

[32] S.S. Parikh, D. Ruiz, H. Kalva, G. Fernández-Escribano, V. Adzic, High bit-depth medical image compression with HEVC, IEEE J. Biomed. Health Inf. 22 (2) (2018) 552–560, https://doi.org/10.1109/JBHI.2017.2660482.
[33] S. Golomb, Run-length encodings, IEEE Trans. Inf. Theory 12 (1966) 399–401.
[34] I.H. Witten, R.M. Neal, J.G. Cleary, Arithmetic coding for data compression, Commun. ACM 30 (6) (1987) 520-540, https://doi.org/10.1145/214762.214771.
[35] J. Duda, K. Tahboub, N.J. Gadgil, E.J. Delp, The use of asymmetric numeral systems as an accurate replacement for Huffman coding. 2015 Picture Coding Symposium (PCS), 2015, pp. 65–69, https://doi.org/10.1109/PCS.2015.7170048.
[36] H. Everett, Generalized lagrange multiplier method for solving problems of optimum allocation of resources, Oper. Res. 11 (3) (1963) 399–417, https://doi.org/10.1287/opre.11.3.399.
[37] Y. Shoham, A. Gersho, Efficient bit allocation for an arbitrary set of quantizers (speech coding), IEEE Trans. Acoust. Speech Signal Process. 36 (9) (1988) 1445–1453, https://doi.org/10.1109/29.90373.
[38] K. Ramchandran, A. Ortega, M. Vetterli, Bit allocation for dependent quantization with applications to multiresolution and MPEG video coders, IEEE Trans. Image Process. 3 (5) (1994) 533–545, https://doi.org/10.1109/83.334987.
[39] D. Valsesia, E. Magli, A novel rate control algorithm for onboard predictive coding of multispectral and hyperspectral images, IEEE Geosci. Remote Sens. Lett. 52 (10) (2014) 6341–6355.
[40] M. Conoscenti, R. Coppola, E. Magli, Constant SNR, rate control, and entropy coding for predictive lossy hyperspectral image compression, IEEE Trans. Geosci. Remote Sens. 54 (12) (2016) 7431–7441, https://doi.org/10.1109/TGRS.2016.2603998.
[41] D. Valsesia, E. Magli, Fast and lightweight rate control for onboard predictive coding of hyperspectral images, IEEE Geosci. Remote Sens. Lett. 14 (3) (2017) 394–398.
[42] M. Blum, R.W. Floyd, V. Pratt, R.L. Rivest, R.E. Tarjan, Time bounds for selection, J. Comput. Syst. Sci. 7 (4) (1973) 448–461.
[43] Lossless Multispectral & Hyperspectral Image Compression, CCSDS 123.0-B-2 Blue Book, February 2019.
[44] N. Jayant, P. Noll, Digital Coding of Waveforms, Prentice-Hall, 1984.
[45] I. Blanes, E. Magli, J. Serra-Sagristá, A tutorial on image compression for optical space imaging systems, IEEE Geosci. Remote Sens. Mag. 2 (3) (2014) 8–26.
[46] National Cancer Institute, National Institute of Health, The Cancer Genome Atlas, 2023, https://cancergenome.nih.gov/.
[47] Single-Pass Rate Control with Lossless Region of Interest Coding Implementation, 2023, http://gici.uab.cat/GiciWebPage/downloads.php.
[48] J. Bartrina-Rapesta, Pathology Imaging and Region of Interest Mask Definition, 2020, 10.21227/afgq-ht69.
[49] HM16.9 Software, 2023, https://hevc.hhi.fraunhofer.de/svn/svn_HEVCSoftware/tags/HM-16.9/.
[50] D.A. Clunie, 2023, https://www.dclunie.com/jpegls.html.
[51] J. Bartrina-Rapesta, M.W. Marcellin, J. Serra-Sagristá, M. Hernández-Cabronero, A novel rate-control for predictive image coding with constant quality, IEEE Access 7 (2019) 103918–103930, https://doi.org/10.1109/ACCESS.2019.2931442.